Microcirculation, 13: 15–32, 2006

ISSN: 1073-9688 print / 1549-8719 online
DOI: 10.1080/10739680500383407

Taylor & Francis
Taylor & Francis Group

A Novel Three-Dimensional Computer-Assisted Method for a Quantitative Study of Microvascular Networks of the Human Cerebral Cortex

FRANCIS CASSOT,* FREDERIC LAUWERS,† CÉLINE FOUARD,‡ STEFFEN PROHASKA,§ AND VALERIE LAUWERS-CANCES¶

*Functional Neuroimaging Laboratory, INSERM U455, CHU Purpan, Toulouse, France; †Department of Anatomy, LSR 44, Faculty of Medicine Toulouse-Purpan, Toulouse, France; ‡Epidaure, INRIA, 2004, Sophia Antipolis, France; §Zuse Institute Berlin (ZIB), Berlin-Dahlem, Germany; and ¶Department of Epidemiology and Public Health, Faculty of Medicine, Toulouse, France

ABSTRACT

Objective: Detailed information on microvascular network anatomy is a requirement for understanding several aspects of microcirculation, including oxygen transport, distributions of pressure, and wall shear stress in microvessels, regulation of blood flow, and interpretation of hemodynamically based functional imaging methods, but very few quantitative data on the human brain microcirculation are available. The main objective of this study is to propose a new method to analyze this microcirculation.

Methods: From thick sections of india ink-injected human brain, using confocal laser microscopy, the authors developed algorithms adapted to very large data sets to automatically extract and analyze center lines together with diameters of thousands of brain microvessels within a large cortex area.

Results: Direct comparison between the original data and the processed vascular skeletons demonstrated the high reliability of this method and its capability to manage a large amount of data, from which morphometry and topology of the cerebral microcirculation could be derived.

Conclusions: Among the many parameters that can be analyzed by this method, the capillary size, the frequency distributions of diameters and lengths, the fractal nature of these networks, and the depth-related density of vessels are all vital features for an adequate model of cerebral microcirculation.
Microcirculation (2006) **13,** 15–32. doi:10.1080/10739680500383407

KEY WORDS: cerebral microcirculation, confocal microscopy, human brain, morphometry, segmentation

In the field of microcirculation, the lack of precise anatomic 3-dimensional data is a continuing problem. Detailed information on microvascular network anatomy is required for understanding several aspects of circulatory system function. Distributions of pressure and wall shear stress in microvessels (52) and transport and exchange of oxygen and other materials in physiological systems (6,46) are tightly coupled with the microvascular architecture. Regulation of blood flow and acute or long-term structural adaptations of vascular beds in response to the functional demands of the tissue (50,51,57), angiogenesis, and remodeling (35) or the end-organ damage associated with hypertension (36), as well as the blood flow response to physical or neural activity, and, subsequently, the interpretation of hemodynamically based functional imaging methods (2,24,37,63) are determined by the anatomy of the microcirculation. In all these fields many investigators have pointed out the crucial influence of network structure and it has been claimed that "future progress will require not only investigation of molecular and cellular mechanisms but also network-level studies that show how

This work was partially supported by grants n° 00 H 0587 from the Fonds de la Recherche Technologique of the French Department of Research and Technology and n° 02 TS 031 of the French Department of Education Research and Technology. The authors are greatly indebted to Henri Duvernoy who placed his wonderful collection of injected human brains at our disposal and gave us precious indications. We thank Philippe Cochard and Brice Ronsin for their help in the use of confocal microscopy at the Centre de Biologie du Développement of Université Paul Sabatier, Toulouse, and Grégoire Malandain at INRIA and Malte Westerhoff from Mercury Inc., for their help in the development on the central lines extraction algorithms. The authors also express their thanks to Prasanna Puwanarajah for revising the English language of the manuscript.

Address correspondence to Dr. Francis Cassot, INSERM U455, Service de Neurologie, CHU Purpan, 31059 Toulouse Cedex 3, FRANCE. E-mail fcassot@toulouse.inserm.fr

Received 30 April 2005; accepted 7 July 2005.

these mechanisms are integrated in a physiological context'' (66).

A wealth of data on vascular anatomic structure has emerged in recent years, lending itself toward a comprehensive database of knowledge of microcirculatory physiology (48). Particular attention has been paid to some intraorgan circulations, such as the coronary and pulmonary microvascular networks. Kassab and co-workers (27–29) have developed several innovations to study the morphometry of vascular trees, which have been used to isolate the anatomy of the porcine coronary circulation, yielding a complete set of morphometric data on the entire coronary vasculature in that species. The utility of these methods in describing the quantitative anatomy of intraorgan vasculature is evident and these advancements in morphometry along with the automation of vascular tree reconstruction, data analysis, and hemodynamic applications should make the database on intraorgan vasculature more abundant and more useful. However, one of the problems in quantifying very complex networks is that there is no fully automated image segmentation method that provides the necessary accuracy. Thus, for imaging or casting methods, some subset of the data obtained with semiautomated methods must be used to extrapolate the whole (26).

By contrast with other organs, few quantitative data concerning human microvascular cerebral networks are currently available in the literature. Most of them have come from anatomic studies using injected specimens, which provide only morphological characteristics of the main vessels with some morphometric data summarized to mean diameters and lengths of global arborescences. Discrepancies between arterial and venous vessels remain a problem, since there is no quantitative information about the capillary network.

Most of our knowledge of human cortical vessels comes from the work of H. Duvernoy. He has delineated the main morphological features of arteries and veins from the pial network to the deep cortical layers (13). However, topologic data are still needed. Duvernoy described a possible functional vascular unit represented by a central vein surrounded by a wreath of several arteries. Some authors (54) have suggested that the capillary bed is a continuous network arranged parallel to the cortical surface without any functional organization. Others suggest the existence of a regulating system based on observations of perivascular structures and blind endings (18,55).

One of the most striking features of the human brain microcirculation is its high geometric complexity associated with its fully three-dimensional nature. As such, microvascular networks from the cerebral cortex do not lend themselves well to the Krogh description (7).

Comparison between the results given by 2D and 3D morphometry has shown that only 3D morphometry is able to obtain reliable data on highly complex vascular networks and that 2D morphometry should be limited to the analysis of flat two-dimensional vascular networks to prevent underestimation of parameters (41).

The purpose of this study is to introduce a 3D computer-assisted method for microvascular cerebral network analysis. Some results on the morphometry and topology of the human brain microcirculation are presented here to illustrate the potential value of this method.

MATERIALS AND METHODS

A digital three-dimensional image of the network was obtained from thick sections (300 μm) of india ink-injected human brain (Duvernoy collection) (Figure 1a) by confocal laser microscopy (Microscope Zeiss LSM 410—Laser 543 nm—Objective Zeiss Plan-Apochromat, magnification 20×, numerical aperture 0.75). The collateral sulcus in the temporal lobe (Figure 1b) was the anatomical region chosen for this study because of the outstanding quality of the injection in this area. A linear encoder (Heidenhain LS406C and display unit ND720) was used to quantify the exact displacement of the microscope table. It allowed precise movement of the specimen with an accuracy of approximately 5 μm. The entire volume of the cortex on both sides of the sulcus was digitized. Each elementary block contained 70 sections (512 × 512 pixels), each one separated by a distance of 3 μm. Horizontal displacements were smaller than the matrix size to simplify the mosaic construction; these had an overlap of about 50 voxels. Data for all the blocks were stored on a hard drive to be associated later in the process.

The coordinates of the left upper corner measured by the positioning system were registered as well as the voxel size (typically $1.22 \times 1.22 \times 3$ μm). Each block was preprocessed: a 2D median filtering reduced salt-and-pepper noise induced by the microscope and a 3D Gaussian filtering smoothed vessels borders.

Furthermore, to compensate the loss of illumination in the lowest slices, this operation performed a

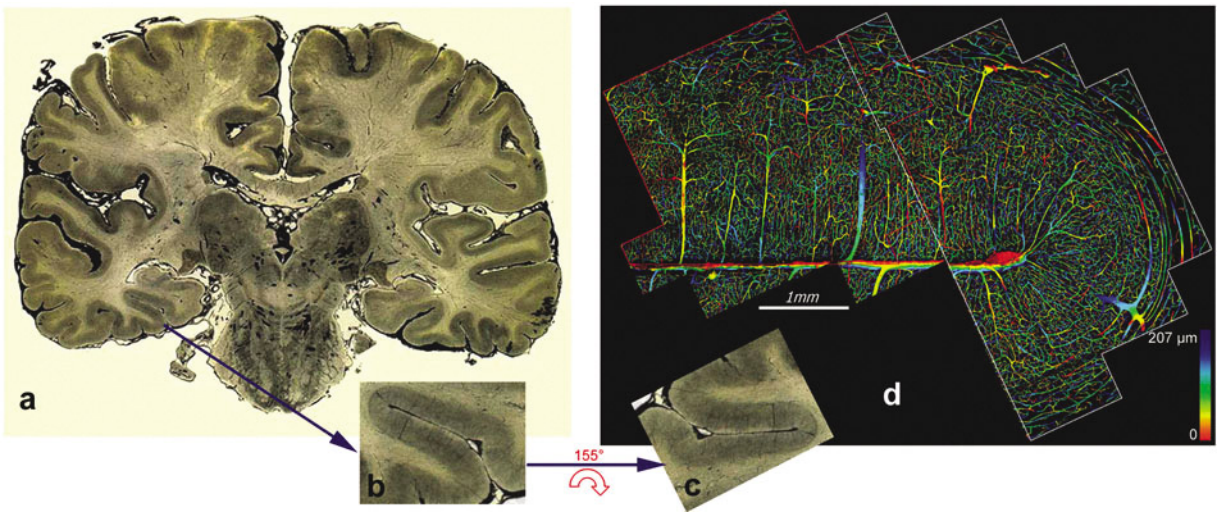

Figure 1. A thick section of india ink-injected human brain used for data acquisition: (a) general view; (b, c) the collateral sulcus in the temporal lobe; (d) depth coded projection of the zone reconstructed by confocal microscopy with the outlines of mosaics M1 and M2.

prethresholding of the data depending on the depth z and was defined for each point by $A = a(a > s(z))$, where a is the data value for a point (x, y, z), and $s(z)$ is a function of z. In practice, $s(z)$ is an increasing linear function of z. The same arithmetic function was applied to all the blocks.

The individual bricks covering a large zone were then added in a special data object called an image mosaic, which stores only links to files on disk (Figure 1d). The data blocks gathered in a mosaic were then realigned using a correlation technique: the image positions were reestimated by optimizing a similarity measured on the overlapping area of about 50 voxels between the mosaic images. This ensures that the vessels in the overlapping area matched perfectly as well as correcting imprecise relative block positions due to the x-y positioning system.

The image mosaic contains a large quantity of data (typically several gigabytes), and cannot be loaded and processed at once in the memory of a standard computer. Adapted methods should be proposed to adequately process such images.

First, a large disk data object was created. In this way, the 3D visualization software Amira (Mercury TGS, Merignac, France, San Diego, USA, Zuse Institute, Berlin, Germany) (60) is able to manage a volume of data larger than the computer main memory. It also allows the extraction of subvolumes and the subsequent visualization of these using standard or advanced 3D visualization techniques provided by Amira.

The next stage is to extract vessel center lines. Indeed, center lines are compact representations of data. They give direct information on network topology and vessel directions, lengths, and junctions. Moreover, if augmented with distance map, they also give information on vessel radii, diameters, and density. To do so, we developed algorithms adapted to large disk data sets. Their main feature and advantage is that they process data locally while preserving global properties. The methodology used is detailed in Appendix A. Note that the distance map measures the distance between any point inside a vessel to the nearest vessel wall in any direction. For a center line point this provides a good estimation of the vessel radius in a particular point of its trajectory.

Finally, this algorithm gives a representation of the vascular network as a set of cylinders centered at the center line points (Figure 2), the radii of which correspond to the distance map values at these points. This lineset can be visualized and superimposed to different types of 3D visualization of the original confocal microscope images (Iso-surface, volume rendering, projection views with a color scale) for representation and control purposes. In addition, the lineset can be edited. For further processing of the morphometric data and analysis of the topology it is also stored in an ASCII file. Each line of this file corresponds to a center line point and contains the number of the vessel segment, i.e., a blood vessel between two successive points of bifurcation, the x, y, z coordinates of the point, and the radius of the vessel at this point.

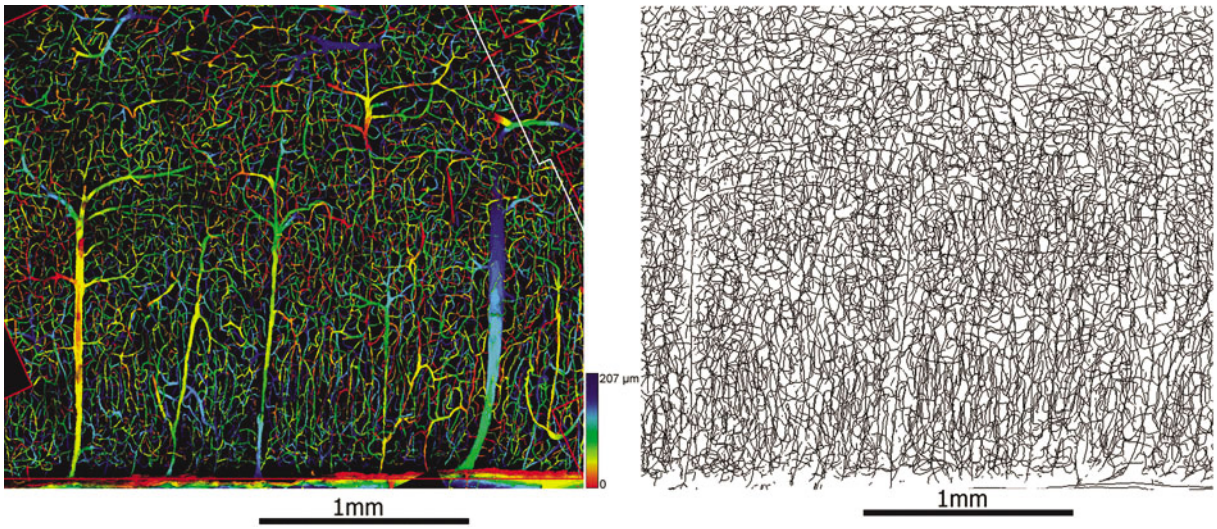

Figure 2. Illustration of the segmentation process in part of the M1 mosaic: (left) depth-coded projection of the reconstructed mosaic; (right) corresponding skeleton.

A background distance map is also constructed. For every point outside the vascular structure (i.e., for any point of the brain tissue), this distance map measures the distance from this point to the nearest vascular wall. Subsequently, the following information on the brain microvascular network morphometry can be derived straightforwardly from the lineset: statistical distributions of vascular length and diameter, volume and surface densities, vessel tortuosity and orientation, diameter ratio, and branching angles.

The topological structure of the cerebral arterioles and venules is tree-like, while that of the capillaries is net-like. Because of this essential difference in nature, the topology of these branching or mesh structures should be analyzed separately. We adopted the following strategy to extract a vascular tree from the complete network: after identifying its origin in the sulcus, we traced automatically all the paths from this origin through vessels in which resistance to flow is lower than a prescribed value. The resistance of a vessel segment was estimated according to Poiseuille formula with the relative apparent viscosity of blood flowing through microvessels, taking into account the Fahraeus and Fahraeus-Lindqvist effects (49), assuming an approximately constant hematocrit of 0.45, as a rough approximation (Figure 3). The branching pattern of the arteriolar and venous trees extracted is best described by the diameter-defined Strahler system introduced by Kassab et al. (28). This description assigns an order number to every vascular segment. This ordering scheme starts with order 0 for the "terminal" vessels. When two segments of the same order n meet each other, the confluent is called a vessel of order $n+1$ if, and only if, the diameter of the confluent segment is greater than $[(D_n + \mathrm{SD}_n) + (D_{n+1} - \mathrm{SD}_{n+1})]/2$, where D_n and SD_n denote the mean and standard deviation of the diameters of the vessels of order n. In many instances, several vessel segments of the same order are connected in series: their combination is called an element. The manner in which vessels of one order number are connected to vessels of another order number can be represented by a connectivity matrix. The total number of elements of the same order and their mean diameter and length can be calculated and their variations with the order number described.

Microvessel Density and Orientation

The net-like "capillary" network was then separated from the tree-like structure by thresholding the vessel diameter under a prescribed value. This threshold was fixed to 9 μm according to the mean diameter of the order 0 (terminal) elements defined by the previous analysis of the arterial and venous trees. Vascular volume can be computed directly from the lineset data. Values of the microvessel volume density (MVD) were derived on a frame (3D grid) with a box size of $60 \times 60 \times 120$-μm side lengths. They were defined as the ratio of the total volume of the vessels contained in each box to the volume of the box. These measures were done on two populations: the complete network, including tree-like vessels, and the capillary network, excluding these vessels.

Many authors emphasized a highest capillary density in the middle cortical layers characterizing sensory

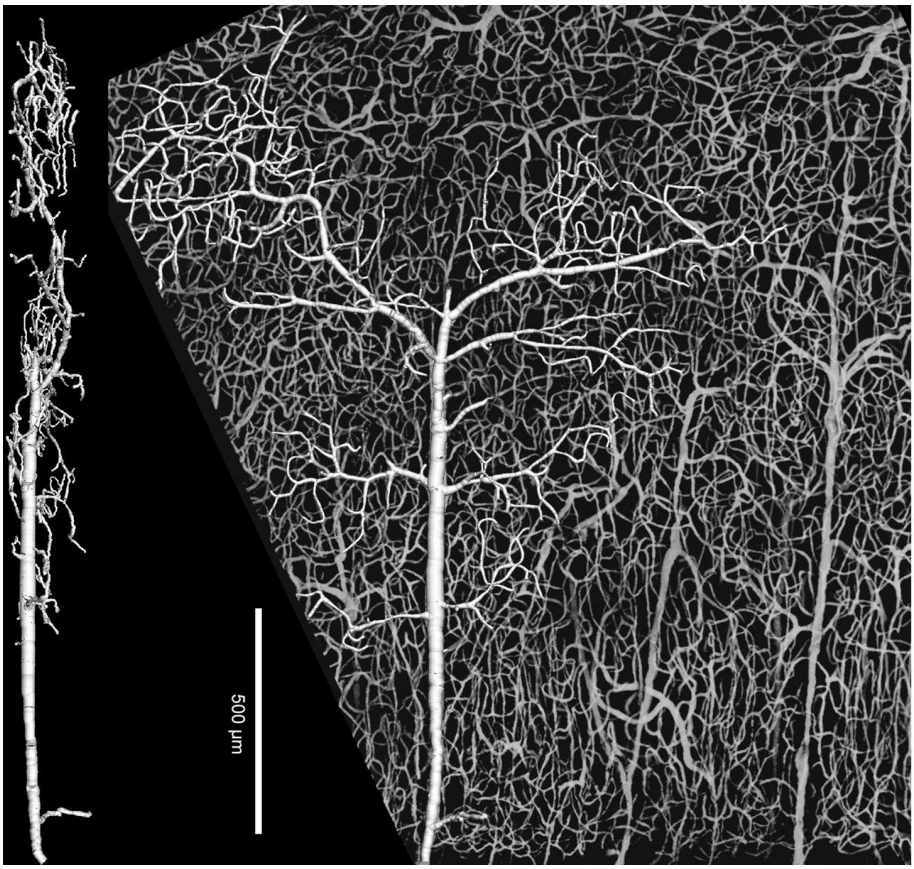

Figure 3. A large vein extracted from the network: (left) side view; (right) top view superimposed on a maximal intensity projection of the mosaic.

cortex. To verify and quantify more precisely these findings we rotated the skeletonized vascular network so that the x axis was parallel to the sulcus. The grid of boxes used to compute these microvessel densities was defined such that their centers were located at planes $y = y_n$, where $y_n = n\Delta y$, with $\Delta y = 30$ μm. On this set of overlapping boxes, a map of MVD was drawn and the mean values of these densities were derived for each y_n.

To analyze these results the cortical thickness was evaluated by 2 different methods. The *vascular cortex* was defined first from the sulcus surface to the point where the vascular density was less than 50% of the mean value, and additionally from the surface to the point where the greater part of the vessels were parallel to the sulcus.

The orientation of the vessels was analyzed on the same grid. These orientations range between 0 and 180 degrees. We divided this range into 24 intervals of 7.5° and plotted their frequency distribution in the volume or subvolume considered. The frequency was estimated as being the ratio of the total length of all the subsegments within a given interval to the total vascular length in the domain considered. We defined a preferential orientation as the peak frequency orientation. The interquartile range (between the 25 and 75% quartiles) of this frequency distribution provided a measure of the orientation heterogeneity. The smaller this range, the more uniform the vessel orientation. The larger, the more heterogeneous, a value of 90° would mean that all orientations are equally probable.

Extravascular Distance

The background distance map (see above) gives the complete distribution of distances from any arbitrary point in the tissue to the nearest vessel. From this map not only the mean and maximal diffusion distance but also the variability in capillary spacing can be inferred. The distances were analyzed on the 3D frame of parallelepiped boxes as defined above. For each box, these distances were plotted as a frequency distribution curve from which the maximal (MDD) and median (mDD) diffusion distance (the

95th percentile and 50th percentile, respectively) and the standard deviation could all be calculated. Taken together, these can be used as an index of variation or heterogeneity of spacing. Such parameters are much more appropriate indices of the oxygen-diffusion distance than either capillary density or intercapillary distance.

Fractal Analysis

The fractal dimension (D_f) can be a valuable parameter to globally assess the microvascular architectural complexity. It was estimated using the box counting method, which consists of overlying the object with a series of 3D grids of decreasing block size. For each grid of box side length ℓ the number of blocks intersected by the structure N_ℓ was counted. The box-counting fractal dimension is given by

$$D_f = \lim_{\ell \to 0} \frac{\log N_\ell}{\log(1/\ell)}$$

where ℓ is the side length of the box and N_ℓ is the smallest number of boxes of side length ℓ required to completely cover the vessel network. In practice, the dimension was obtained by taking the slope of the graph of $\log N_\ell$ against $\log(1/\ell)$, where the box side length was divided by 2 at each successive counting sequence.

In practice, this fractal analysis was applied to regions of interest (ROI) extracted from the 3D image mosaic after the thresholding step. After an edge-detection algorithm using a Sobel filter (ImagePro, Media Cybernetics, Silver Spring, MD, USA) was applied to the ROI, the bilevel images blocks contained only the vessel walls voxels. The smallest boxes were obtained by merging 4 adjacent image voxels and these had a minimal side length ℓ of 3 μm. The counting was stopped after the sixth sequence when the box side length was 32 times that of the smallest box. Above this sequence the network becomes volume filling. In fact, the microvascular fractal dimension (MFD) of a given ROI was estimated after averaging the value of D_f on 16 neighboring blocks of the biggest size. The chosen ROI did not include very large vessels. The ROI centers were located from the sulcus to the white matter throughout the entire depth range.

RESULTS

Validation

In this study we were able to produce a complete automatic reconstruction of the vascular network. We assembled two connecting mosaics in this zone. The first one (M1) stretched along the lateral part of the collateral sulcus (fusiform gyrus), where the main vessels were parallel and orientated normally to the sulcus. In this region, both the sulcus and the outer boundary of the cortex were rectilinear. This mosaic was made of 27 blocks and covered a surface of 7.7 mm^2 with a volume of 1.6 mm^3. The other mosaic (M2) was located at the end of the sulcus, where the outer boundary of the cortex is more or less circular and the main vessels were arranged radially (plicature zone). This second mosaic was made of 34 blocks and covered a surface of 10.4 mm^2 with a volume of 2.15 mm^3. Each mosaic contained a large quantity of data (see Table 1) too large to be managed simultaneously within the computer memory: the depth-coded projection view presented on Figure 1d was obtained after subsampling the data in all directions.

Both skeletons extracted from these mosaics included more than a million data points (Table 1). The 3D coordinates of the vessel central line and its diameter were sampled. This process produced a data lineset of nearly 30,000 vascular segments with an average number of 37 points per segment spaced out by less than 2 μm.

While the average segment length was close to 60 μm for both mosaics, the total lengths and the number of vascular segments by unit volume were slightly higher in the M1 region than in the M2 region. However, they were of the same order of magnitude: 8000 segments and half a meter per mm^3. Note also that the skeletonization process results in a large data

Table 1. Global characteristics of the mosaics, skeletons, and morphometric parameters

Mosaic	M1	M2	M1 + M2
Number of bricks	27	34	61
Number of Segments	14,099	15,250	29,349
by mm^3	8,817	7,219	7,826
Sampled points	503,025	588,447	1,091,472
by mm^3	314,587	273,696	291,059
Total length (mm)	798.32	946.01	1744.33
by mm^3	499.26	440	465
Segment mean length (μm)	56.6	62	59.4
Sampled points/elements	36	38	37
Mean point distance (μm)	1.6	1.6	1.6
Vascular volume (mm^3)	0.0392	0.0523	0.0915
(% of total volume)	(2.45)	(2.43)	(2.44)
Vascular surface (mm^2)	8.66	11.47	20.13
(vasc. surface by mm^3)	(5.42)	(5.33)	(5.37)

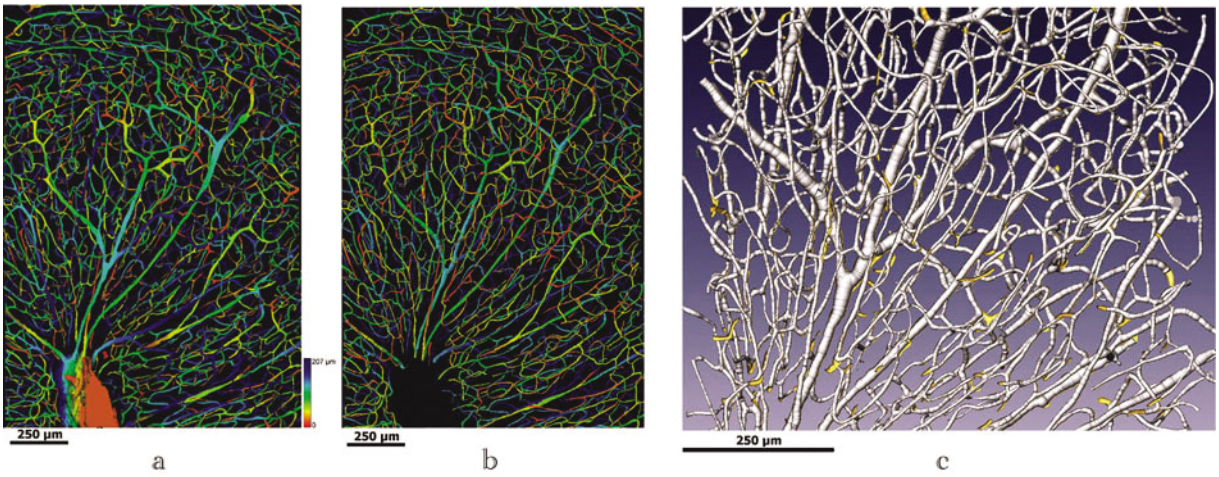

Figure 4. Comparison of the reconstructed network with the original data: (a) projection view of the mosaic; (b) depth-coded visualization of the line set after segmentation; (c) 3D visualizations of the line set (white cylinders) and the original data (yellow isosurfaces).

compression: both skeletons were stored in files of approximately 11 megabytes and could be easily loaded, edited, and visualized. However, in spite of this large compression factor, the skeletons or linesets appeared to keep all the useful information on the vascular network architecture contained within the original raw data.

Validation was obtained either by comparing the original depth-coded projection view to those reconstructed from the skeleton as displayed in Figure 4a, b, or by superimposing the 3D vascular network obtained from the lineset to the isosurface representation of the real data (Figure 4c). Such comparison allows us to check the extracted center lines, but by using the functions of the Amira's Lineset Editor, which enables us to delete, split, or connect lines or points in a network, corrections can be applied interactively when necessary.

While this comparison seemed to be acceptable, it was only visual and, therefore, qualitative. A more quantitative and less subjective assessment of the segmentation method could be achieved from a first analysis of the lineset characteristics as displayed in Table 2. The disconnected (or disrupted) segments represented about 3% (respectively, 8%) of all the segments. This was a nonnegligible proportion, which meant that a complete extraction of the full vascular network had not been fulfilled. On the other hand, this meant that nearly 90% of the vascular architecture had been described correctly. Various factors explain this anomaly: for example, incomplete filling of the vessel, insufficient contrast between the vessel and the surrounding tissue, as well as physiological or pathological (lacunar) vascular endings. Furthermore, these proportions were not homogenous: they increased with the depth of the brain section considered, as the S/N ratio decreased, and varied from about 2% (or 6%) for the disconnected (respectively disrupted) segments in most of the sections ($z < 150\ \mu$m) to more than 6% (respectively, 15%) in the deepest sections ($z > 170\ \mu$m). Another objective argument in favor of the suitability of the segmentation was the negligible amount (less than 1%) of multiple-connected nodes, which are most probably due to artifactual noise.

Global Morphometry

As shown in Table 1 the mean values of volume density and surface density were remarkably similar for

Table 2. Main characteristics of segment and node connectivity for both skeletons

Mosaic	M1	M2	M1 + M2
Unconnected segments (%)	4.1	1.25	2.6
End points segments	10.2	6.2	8.1
Simple nodes (1 daughter branch)	1.2	0.4	0.7
Bifurcations (2 daughter branches)	94.1	94.5	94.4
Trifurcations (3 daughter branches)	4.1	4.5	4.3
Multiple nodes (4 or more daughter branches)	0.6	0.5	0.6

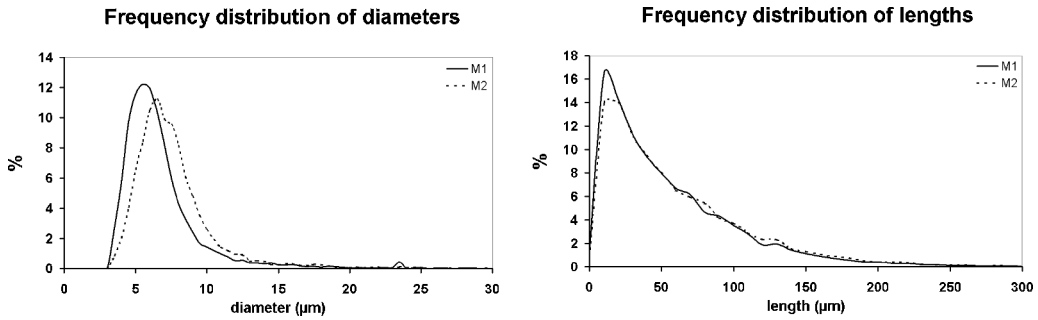

Figure 5. Histograms of diameters (left) and lengths (right) of the complete network for mosaics M1 (solid lines) and M2 (dotted lines).

both mosaics in spite of their visual architectural difference. While this result was a rather coarse characterization of the vascular density, it is worth noting that the apparent difference in the geometrical arrangement of the vessels in these adjacent regions of the cortex did not change their global density. Of course, this does not preclude the possibility that there are local variations within these regions (see below) or regional differences between different regions of the cortex.

Figure 5 displays the frequency distributions of diameter and length for both mosaics. Table 3 summarizes the main characteristics of these distributions, of which none was normal. Distributions of the complete networks were asymmetric with a large positive skewness and a leptokurtosis. However, for these networks the logarithm of the length and the inverse diameter showed normal distributions with similar mean and median, skewness close to zero and kurtosis close to 3. The diameter distributions of capillaries networks were close to normal. Comparisons between both mosaics were made after data transformation when necessary and showed that all distributions were significantly different ($p < 10^{-4}$). However, these differences were very small, as shown on graphic representations.

Main (tree-like) Vessels Topology

Figure 6a displays the branching pattern of typical cortical vein arborescence according to the diameter-defined Strahler system. A total of 5 orders of vessels lie between the postcapillary venules and the piemerian origin in the sulcus. The semilog plot of Figure 6b shows the relationship between the total number of elements N_n and the order number n. Figure 6c shows the relationship between the mean vessel diameter D_n (respectively, the mean vessel element length L_n) and the order number. The curves in these figures can be fitted by equations of the form

$$\log X_n = a + bn$$

where X_n represents D_n, L_n, or N_n, and a and b are constants. b is positive for D_n and L_n, which increase with the order number, and negative for N_n, which decreases with this order. The constants a and b are listed in Table 4 as well as the correlation coefficient

Table 3. Characteristics of the diameter and length distribution functions of the vascular populations under consideration

	M1				M2			
	Complete network		Capillaries		Complete network		Capillaries	
	Diam	Length	Diam	Length	Diam	Length	Diam	Length
Mean	6.91	56.65	5.91	57.37	7.72	61.80	6.56	63.26
Standard deviation	3.85	51.66	1.30	50.98	3.30	56.59	1.27	53.73
Median	6.07	42.03	5.81	43.07	7.05	45.73	6.58	48.08
Interquartile range	5.04/ 7.45	19.70/ 78.03	4.90/ 6.82	20.25/ 79.62	5.90/ 8.50	22.15/ 84.34	5.64/ 7.57	23.93/ 87.13
Skewness	6.02	2.78	0.27	2.68	4.05	2.84	−0.15	2.20
Kurtosis	62.18	25.69	2.38	26.71	34.17	19.92	2.29	15.19

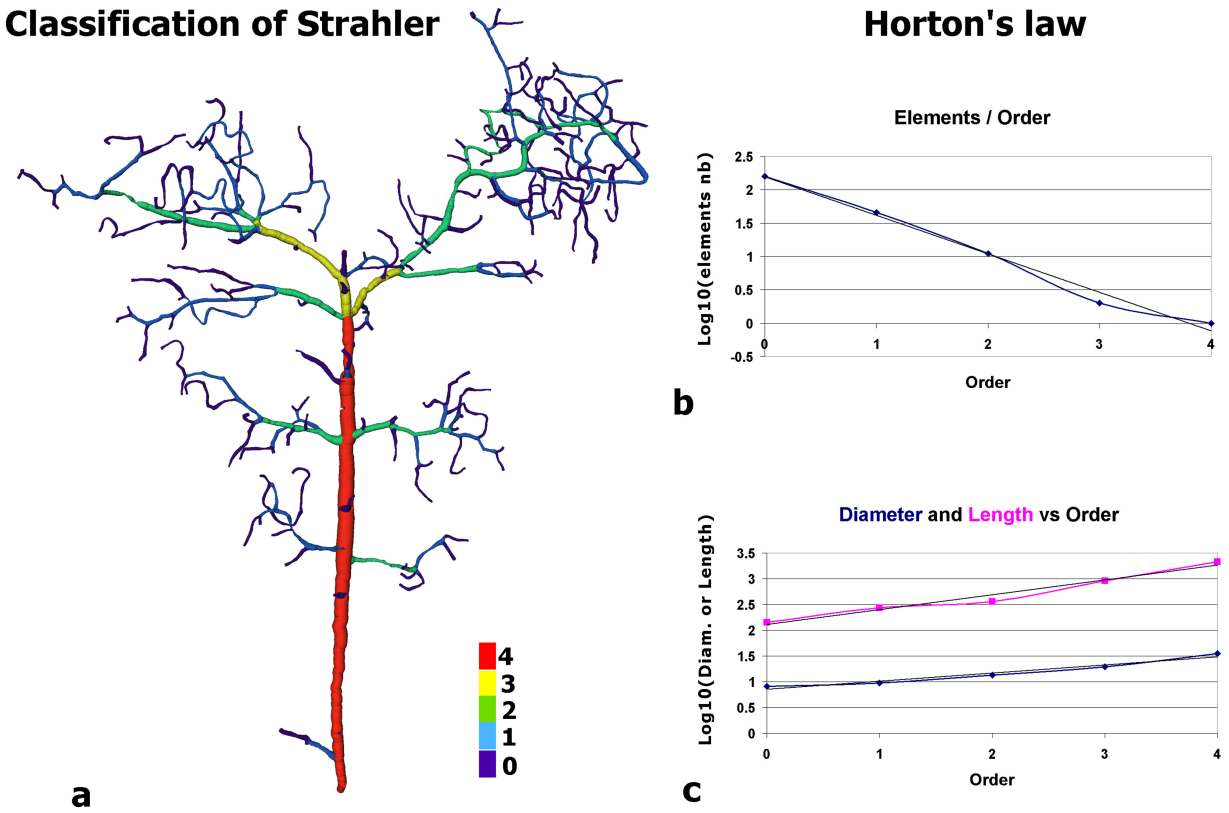

Figure 6. The branching pattern of a large cortical vein according to the diameter-defined Strahler system: (a) the vein with its elements of different orders; (b) the number and (c) the average diameter and length of vessel elements of successive orders.

R^2 of the fitted curves, close to unity, and the diameter (D_n/D_{n-1}), length (L_n/L_{n-1}), and number (N_{n-1}/N_n) ratios, which are constants independent of $n(D_n/D_{n-1} = 10^b)$. This equation is known as Horton's law and a system obeying such a law is fractal.

Net-like Vessels (capillary) Topology

This part of the study was carried out on M1 because of the real perpendicular orientation of the vessels to a rectilinear cortical surface. The following results catalogue 2 samplings of vessels. One, called a *capillary network*, included vessels with a diameter less than 9 μm (this value corresponds to the mean diameter of the order 0 in the Strahler classification) and the other, called a *complete network*, included all vessels.

Table 4. Empirical constants, coefficients of regression and ratios for the relationships between order number and mean diameter, length, and number of vessel elements for a cortical vein (see text)

	Diameter	Length	Total number (vessel elements)
a	0.8547	2.1138	2.1942
b	0.1582	0.2875	0.5765
R^2	0.9563	0.9711	0.9877
Ratio	1.45	1.94	3.77

In the capillary sample, mean diameter and length were, respectively, 5.9 and 57.4 μm. This characterizes the mean capillary dimensions. On this mosaic (M1) cortical thickness (or depth) was 2.5 mm. Volume–density curves are shown in Figure 7. Four vascular layers were clearly identified:

1. From the surface to 240 μm (9.6% of cortex thickness): a band devoid of capillary followed by a rough increase on vascular density
2. From 240 to 1140 μm (9.6 to 45.6%): vessel density increases slowly to a maximum
3. From 1140 to 2070 μm (45.6 to 82.8%): vascular density decreases slightly
4. From 2070 to 2500 μm (82.8 to 100%): rough decrease until the white mater junction where it appears that vascular density reaches a plateau.

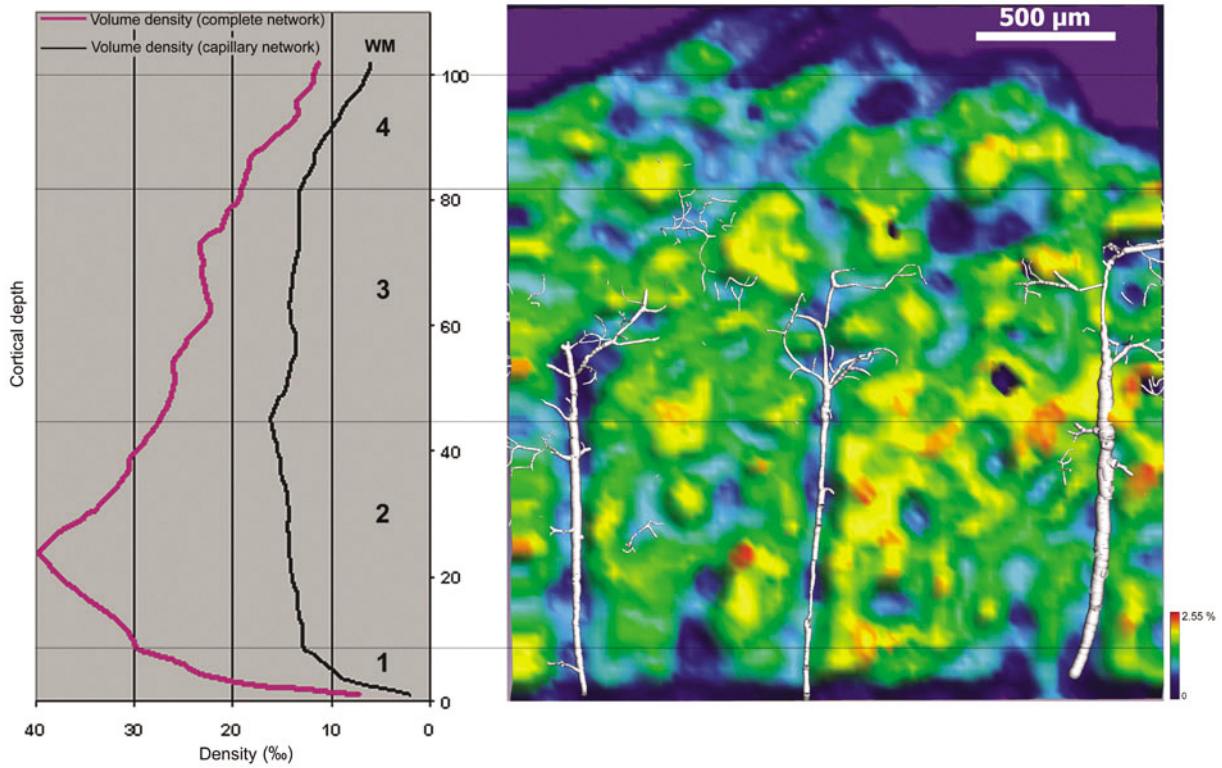

Figure 7. Vascular density of the mosaic M1: (right) height field color-coded representation with the main vessels; (left) the dependency of volume vascular densities, with and without the tree-like network, on the cortical depth.

There is a high vascular density area (>1.4%), ranging from 21.6 to 54% of cortex thickness. A map of capillary density showed an important heterogeneity due to tree-like structures and resulted in a high 40% coefficient of variation. We did not analyze the periodicity of the tree-like vessels in this section.

Segments orientations are shown in Figure 8. The study concerned the capillary network. The most frequent orientation was perpendicular to the sulcus surface (80°). This preferential orientation was clearly seen only into the superficial cortical layers (from 9 to 22% of cortex thickness), where 50% of the vessels are contained in 40° around this preferential value. In the deep cortical layers the orientation became completely unpredictable (50% of the vessels are in a range of 90°) until the white matter where vessels were oriented parallel to the surface. However, mesh geometry was not completely explored in this sample.

Extravascular distances (Figure 9) were studied within the whole network, including arborizations, to introduce a parameter characterizing oxygen diffusion. The curve is linked to the vascular densities by inverse relationship, the greatest vascular density corresponding to the shortest extravascular distance. However, there was no simple mathematical relation between these two parameters, probably because of the variability of mesh geometry, whose distance ranged from 22 to 40 μm, depending of the cortical deepness, and from 22 to 27 μm between 240 (9.6%) and 2200 μm (88%) of cortical thickness. We emphasize that the mean value of the extravascular distance defines the order of magnitude of the mesh (50 μm). The extravascular distance map, with a 17% coefficient of variation, is more homogeneous than the density map. It shows clearly the avascular zone near the pial surface and the avascular space near the more important tree-like structures (Pfeifer space).

Fractal Analysis

The log–log plots of N_ℓ versus $1/\ell$ emphasized highly linear relationships with Pearson coefficients of regression close to 1 (mean value = 0.9984). The slopes of these lines, which define the MFD, ranged from 1.82 for a subcortical ROI to 2.17 for a middle layer

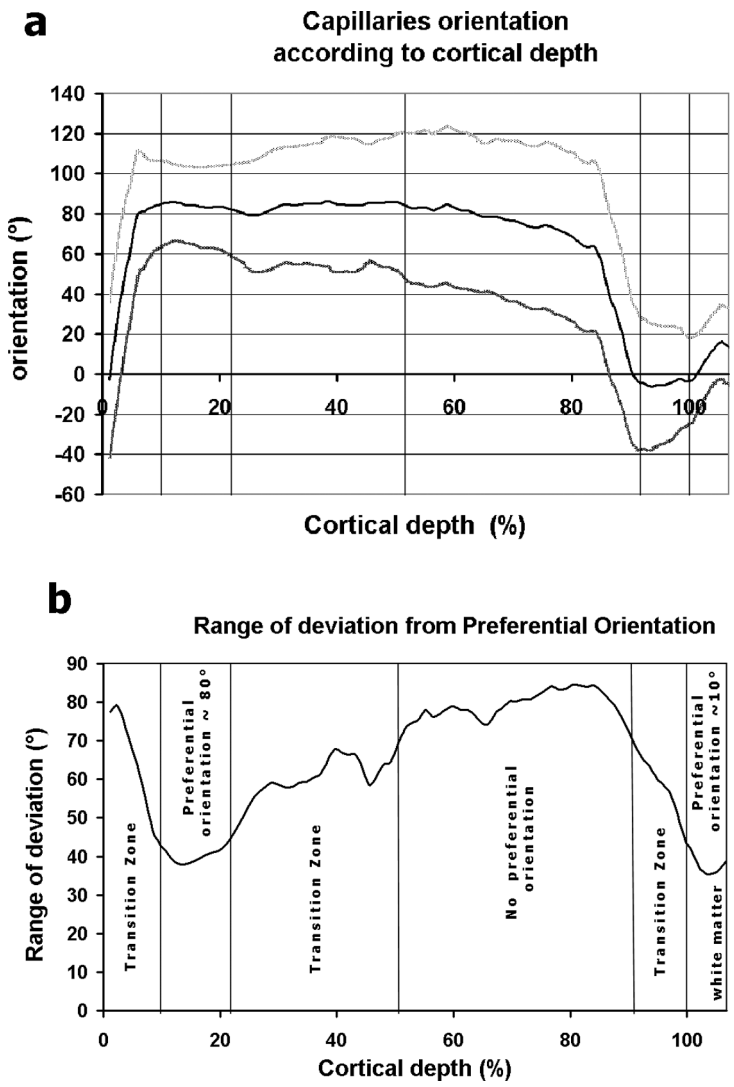

Figure 8. Capillaries orientation according to the cortical depth and range of deviation from the preferential orientation.

cortex ROI with a mean value of 2.03 ± 0.1 (mean $\pm$ SD). The variations of the MFD with the depth were similar to that of the MVD.

DISCUSSION

Anatomical studies of the human cortical vascular network or even work on animal models are usually carried out by direct observation of injected preparation or vascular casts. These methods do not tend to yield quantitative features of the vessels for a number of reasons. Usually, measurements are made manually on a small number of vascular segments concerning one or different parts of the cortex and by using different methods of injection. For a single observer, the geometric complexity of such a vascular network is nearly impossible to deal with in a quantitative manner.

In the light of this, the main objective of this study was to propose a new method by which to analyze the microcirculation of the human brain. From thick sections of india ink-injected human brain, using confocal laser microscopy as a 3D imaging technique, we have developed a new skeletonization algorithm, adapted to a very large data set. It has allowed us to generate a complete and automatic reconstruction of the vascular network, including tens of thousands of vascular segments within a large area of cortex (20 mm^2). Direct comparison between 3D visualizations of the original data and of the processed vascular lineset demonstrated the high reliability of this

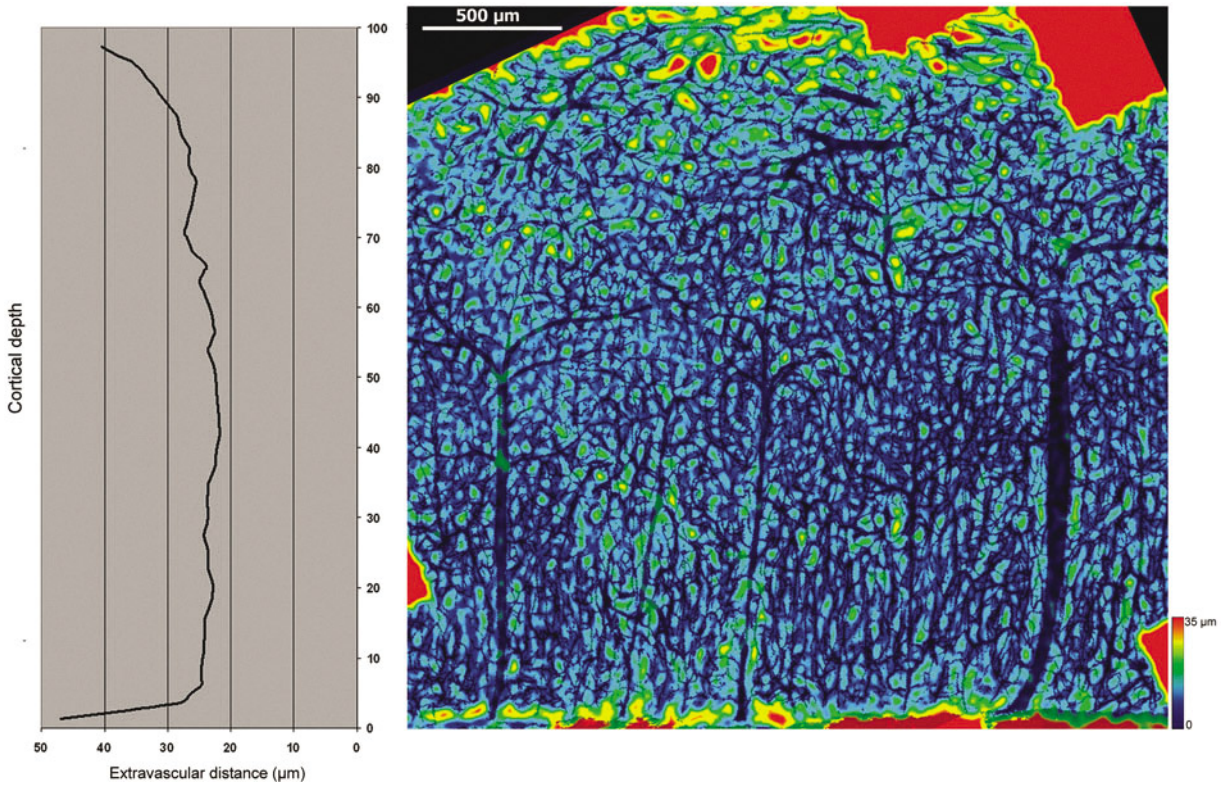

Figure 9. Extravascular distance map and variation of maximal extravascular distance with the cortical depth.

method. Incomplete filling of the vessel or insufficient contrast between the vessel and the tissue as well as pathophysiological vascular endings prevented a 100% full extraction of the vascular network. However, this anomaly was limited and analysis of the data guaranteed that at least 90% of all the vessels were precisely represented. The volume of the data lost could be estimated as being less than 3% of the total vascular volume.

To our knowledge, such a large, quantitative and reliable data library on the microcirculation of the human brain has never before been compiled and could potentially form the first parts of a database that could be analysed and complemented in a larger research project. Though the resulting linesets contained hundreds of thousands of points and tens of thousands of lines, its memory sizes did not exceed a number of megabytes and could be easily loaded, visualized, and edited on a PC. This demonstrates that the skeletonization algorithm proved capable of generating a large "compression" factor with respect to the raw data. In spite of this, all the useful information was safely preserved for morphometric and topologic analysis.

The material used was of excellent quality but was not completely suited to this acquisition protocol. Tata and Anderson (61) argued that the use of viscous solutions such as india ink in gelatin can cause incomplete vessel perfusion. They tested whether capillaries seen in tissue perfused with fixative, embedded in celloidin, and stained with methylene blue could be a useful alternative for the investigation of brain vascular structure. They concluded that their method provided a vascular quantification comparable to that from india ink-perfused tissue, but they found that the capillary diameter was greater in the celloidin-embedded tissue than in the india ink-perfused tissue and claimed that measuring the diameter between walls provided more accurate measure than the widest distance between india ink pigments. In fact, their measurements were made from 2D light microscope images and, due to the highly 3D nature of the cerebral microvascular network, most of vessel segments were not correctly focused. Clearly, such a 2D approach, as well as the presence of pericytes masking part of the vessels and the low image contrast with celloidin, made a reliable reconstruction of the 3D microvascular network impossible.

Better contrast materials, such as mercox casts, improve the isotropy of the vascular network and aid exploration with a more 3-dimensional approach, at

the scale of the arborizations, as shown by preliminary tests. Confocal microscopy is the best way to acquire 3D data. Computer-integrated systems, using manual joystick control of the microscope stage, remain commonly used for 3-dimensional mapping of some microvascular networks (8). Previous attempts (11,32) with this technique demonstrated that it was not appropriate to our objective because it is user-dependent and the time needed for a full data acquisition on such large volumes would be prohibitive.

Corrosion cast scanning electron microscopy studies (13,18,43,54,55) give precise morphologic features, including perivascular structure, but are generally used as a 2D approach insofar as images cannot be easily recorded and treated in the 3 planes of the space as with confocal microscopy (40). Microfocal X-ray computed tomography offers an alternative to casting methods but there is no fully automated image segmentation method that provides the necessary accuracy (26). High-resolution X-ray computed tomography using specific contrast agents (47) seems to give quite interesting results and prospects.

The volume of the samples used in this study seems to be insufficient for a regional approach to the organization of arteries and veins within the cortical microcirculation. On another hand, this volume was well adapted to a first quantitative study of the capillary network.

To illustrate the potential applications of this method, we present data on the morphometry and the topology of the cerebral microcirculation. The reliability of the database allowed us to establish some basic information on the elementary morphometry of cortical microvasculature. Although the discussion of these results goes beyond the methodologic objective of this paper some of them will be briefly commented on hereafter.

Some of the results presented here differ considerably from descriptions in classic anatomical literature and from more recent studies that utilized a qualitative approach when a quantitative one was required. We found here, from a very large amount of data collected on two geometrically different zones, that the mean capillary size varied from 5.9 to 6.5 μm in diameter and from 57.4 to 63.3 μm in length. On the same material Duvernoy evaluated the capillary diameter around 3.5 μm and corrected this measure to around 6 μm on mercox cast and in accordance with other authors. On this issue our results concur with the accepted thinking. We note that the anatomic preparation can modify the diameters of vascular segments mostly because of shrinkage of the sample (61) but these measures vary in vivo, too, and the outcomes of the sample preparation should not change other parameters, such as vascular density and frequency distributions of vascular length and diameter, since this shrinkage is global and homogeneous. We noticed that, for the complete network, the length of vessel segments was best approximated by the log-normal distribution and the inverse of segments diameter was the function that best fitted with a normal distribution. There are very few quantitative data on human brain microcirculation but these results are superimposable with those recorded by Hudetz with an intravital technique in the rat brain (21).

Others animal studies report capillary segments lengths of 10–300 μm (21,25,42–44). The total length by mm^3 was evaluated at 465 mm/mm^3, while it is estimated around 1000 mm/mm^3 by Hudetz (threefold higher than in white matter) and Pawlik et al. (22,44) and measured at 215 mm/mm^3 by Tata and Anderson with the same contrast agent (india ink–gelatin) in the motor cortex of the rat (61). Differences might be obvious between human and rat cortex as variations of vascular density have been often mentioned between motor and sensory cortex in humans (13,18,34).

Turner (63) used an estimated capillary length of 200 μm, which corresponds to an arterio-venous flow path between 2 arborized vessels, and which is four times the result that we observed quantitatively here for a single segment. What is clear is that there exists no real consensus on what a capillary is, anatomically, histologically, or hemodynamically. The Strahler classification allows the identification of the beginning (or the end) of the mesh and its relationships with tree-like vessels. Further studies could profit from this method to precisely define the nature of the arborizations and their topology in the cortex, as arteriovenous discrimination at microregional resolution remains a problem in postmortem studies and the hypothesis of functional organization, or even of a special or regular pattern of arborization is a matter still very much under debate.

Like other microvascular networks, and as underlined by several authors (15,28), the cerebral network is both a branching or tree-like and a mesh or net-like structure. These two parts of the vascular architecture were analyzed separately. The branching patterns of typical cortical arborisation were classified according to the diameter-defined Strahler system. The number of elements, mean diameter, and length for each element order so defined were shown

to obey Horton's laws, which revealed the fractal nature of this network as demonstrated for many other vascular networks (16,20,31,59,62,64,65).

The fractal dimension for a branching network can be expressed in terms of the number and length–order ratios according to Turcotte $D_f = (\log R_N)/(\log R_L)$ (62). It is remarkable that, for the trees considered here, this gives a value of the fractal dimension (2.0) that is nearly identical to the one estimated with the box counting method (2.03) applied to the complete network, which characterizes the mesh part of the network. Moreover, this is the same fractal dimension that is found for the diffusion process. It may have implications for the understanding of the design principles of angiogenesis and its modelling.

These results differ from the values mostly found in the literature (3,27,38). Fractal analyses of the circulation of the normal human retina (38) and of the normal arteries and veins of the mouse skin (3) both lead to a fractal dimension value of 1.7. But, in contrast with the present study, both measures were inferred from networks embedded or projected in two dimensions, which leads to an underestimation of the parameters, as demonstrated by Minnich (41). The relative differences between the number and length ratios found in this study and those found for the pig coronary arterial trees (27) are 10% or less, while being approximately 20% for the diameter ratios. The fractal dimensions that can be inferred from Kassab data vary from 1.78 to 1.96, depending on the coronary artery. For the same arteries, the diameter fractal dimensions vary from 1.99 to 2.09. These values, which are very similar to those of the present study, differ significantly from the 2.99 length fractal dimension reported for the dog pulmonary venous tree or the 2.97 corresponding value for the human pulmonary arterial tree (29).

One of the most striking features of cerebral microcirculation is its heterogeneity. This heterogeneity appears through a global organization in columns limited by the arborized vessels. The depth-related density of vessels is quantitatively demonstrated by the technique presented here. The high density area ranged from 21.6 to 54% of cortex thickness seems to characterize a sensory cortex. If we try to establish a correlation between these results and the cellular structure of the cortex, it appears that it involves a large part of layer III, including IIIb and IIIc, and the entire layer IV. This kind of correlation needs further studies, including an outstanding description of the cyto-architecture of the cortex studied. Many authors have dealt with the relationships between neuronal activity and vascular density (1,13,33). The area on which we focused was located on the lateral aspect of the collateral sulcus on the fusiform gyrus and would correspond from recent fMRI studies to the position of the color vision center (5,39).

It is more difficult to draw conclusions about the use of the orientation of vessels as a discriminative tool for the segmentation of the cortex in vascular layers. A correlation between a preferential orientation and nerve fiber organization could be suggested as explanation.

Oxygen exchanges between blood flowing through the vessels and the brain tissue they supply are of crucial importance for ongoing neural activity. They are the main determinant of the BOLD signal used to emphasize this activity in functional MRI. These exchanges are governed by convection–diffusion equations in a complex geometric configuration and can be modeled using different numerical methods, such as finite-difference approximation (6,17) or Green's function method (19,58). Note that these functions are themselves derived from the elementary solution of the Poisson equation, which, in 3D, is proportional to the inverse of the distances between the tissue and the oxygen sources in the vessels. So, the distribution of what we called the extravascular distance might clearly be a valuable indicator of the capability of the vascular network to respond to the metabolic demands of local neuronal activity. It has been shown to calculate diffusion distances more accurately than an estimation from capillary density (30).

This parameter has a relatively homogenous distribution out of the pial surface, the subcortical layer, and in the neighborhood of the large vessels, where it increases abruptly. It gives also an order of magnitude of the mesh size (50 μm). Further studies are still needed to complete these preliminary results and to characterize the geometry of such a network.

One of the important features of this study was to account for the 3-dimensional nature of the cerebral microvascular network. Vascular network extraction as well as the morphometric and topological results were all collected and processed in 3 dimensions, which seems to us to be a fundamental condition for a complete understanding of microcirculation.

The morphometric characteristics of the human cerebral cortex vascular anatomy are required for a better interpretation of cerebral functional imaging—functional magnetic resonance imaging (fMRI) and

positron emission tomography (PET)—and to generate a network model. At present, "the exact relationship between the measured fMRI signal and the underlying neural activity is unclear" and "the extent of activation in human fMRI experiments is very often underestimated to a significant extent owing to the variation in the vascular response" (37). It is now recognized that "the limit of spatial resolution in fMRI is determined by anatomy of the microcirculation" (24) and that "changes in blood flow propagate downstream in veins and can give rise to spurious activation at sites remote from neuronal activity," leading to "the most severe constraints on the spatial resolution of BOLD contrast MRI" (63).

However, many other fields of research could profit from the present method independently of the species or the organ. The study of microvascular geometry is of particular interest since it affects the oxygen supply (12,17,23,45,46). These types of quantitative works could be helpful to other investigations in microcirculation, including tumor-related neovascularization. The analysis of tumor microvascular complexity measured by parameters such as microvessel fractal dimension has been shown to provide important prognostic information as well as novel insights into the biology of tumor angiogenesis (4,10,56).

CONCLUSION

We have presented here preliminary results of an exciting new mode of analysis of the microcirculation of the human brain. Even though these are early stages, it is clear to us that this method allows a hitherto unattainable level of anatomical and topological resolution that presents itself quantitatively. The capillary size, the frequency distributions of diameters and lengths, the fractal nature of these networks, and the depth-related density of vessels are all vital features for an adequate model of cerebral microcirculation. A more exhaustive analysis of such vascular networks is the next step toward a better understanding of the cerebral vascular bed in a functional sense. At the very least, the construction of realistic hemodynamic models might be undertaken from quantitative features obtained by a suitable mathematical treatment or directly from a realistic 3D segmentation of an adequate volume of cortex.

It is important that these data are delivered using a pertinent set of criteria that are mathematically sound in choice and execution; what we present here, as much as anything, is a demonstration of the power of this method as a new tool. Clearly, establishing a complete model of cerebral microcirculation is an extensive task; this paper presents a description of a new first step, whose potential shall become apparent with time and continuing work.

REFERENCES

1. Argandona EG, Lafuente JV. (2000). Influence of visual experience deprivation on the postnatal development of the microvascular bed in layer IV of the rat visual cortex. *Brain Res* 855:137–142.
2. Arthurs OJ, Boniface S. (2002). How well do we understand the neural origins of the fMRI BOLD signal? *Trends Neurosci* 25:27–31.
3. Baish JW, Gazit Y, Berk DA, Nozue M, Baxter LT, Jain RK. (1996). Role of tumor vascular architecture in nutrient and drug delivery: an invasion percolation-based network model. *Microvasc Res* 51:327–346.
4. Baish JW, Jain RK. (2000). Fractals and cancer. *Cancer Res* 60:3683–3688.
5. Bartels A, Zeki S. (2000). The architecture of the colour center in the human visual brain: new results and a review. *Eur J Neurosci* 12:172–193.
6. Beard DA, Bassingthwaighte JB. (2001). Modeling advection and diffusion of oxygen in complex vascular networks. *Ann Biomed Eng* 29:298–310.
7. Beard DA. (2001). Computational framework for generating transport models from databases of microvascular anatomy. *Ann Biomed Eng* 29:837–843.
8. Bearden SE, Segal SS. (2005). Neurovascular alignment in adult mouse skeletal muscles. *Microcirculation* 12:161–167.
9. Borgefors G. (1984). Distance transformation in arbitrary dimensions. *Computer Vision, Graphics, and Image Processing* 27:321–345.
10. Carmeliet P. (2001). Cardiovascular biology: creating unique blood vessels. *Nature* 412:868–869.
11. Cassot F, Paulin-Laurens P, Plouraboue F, Duvernoy H, Marc-Vergnes JP. (1999). Morphometric study of a human microvascular network. *J Cereb Blood Flow Metab* 19(suppl 1):S708 (Abstr).
12. Chang BL, Yamakawa T, Nuccio J, Pace R, Bing RJ. (1982). Microcirculation of left atrial muscle, cerebral cortex and mesentery of the cat: a comparative analysis. *Circ Res* 50:240–249.
13. Duvernoy HM, Delon S, Vannson JL. (1981). Cortical blood vessels of the human brain. *Brain Res Bull* 7:519–579.
14. Fouard C, Malandain G. (2005). 3-D chamfer distances and norms in anisotropic grids. *Image and Vision Computing* 23:143–158.
15. Fung YC. (1996). *Biomechanics : Circulation.* New York: Springer.
16. Gan RZ, Tian Y, Yen RT, Kassab GS. (1993). Morphometry of the dog pulmonary venous tree. *J Appl Physiol* 75:432–440.

17. Goldman D, Popel AS. (2000). A computational study of the effect of capillary network anastomoses and tortuosity on oxygen transport. *J Theor Biol* 206:181–194.
18. Harrison RV, Harel N, Panesar J, Mount RJ. (2002). Blood capillary distribution correlates with hemodynamic-based functional imaging in cerebral cortex. *Cereb Cortex* 12:225–233.
19. Hsu R, Secomb TW. (1989). A Green's function method for analysis of oxygen delivery to tissue by microvascular networks. *Math Biosci* 96:61–78.
20. Huang W, Yen RT, McLaurine M, Bledsoe G. (1996). Morphometry of the human pulmonary vasculature. *J Appl Physiol* 81:2123–2133.
21. Hudetz AG, Greene AS, Feher G, Knuese DE, Cowley AW Jr. (1993). Imaging system for three-dimensional mapping of cerebrocortical capillary networks in vivo. *Microvasc Res* 46:293–309.
22. Hudetz AG. (1997). Blood flow in the cerebral capillary network: a review emphasizing observations with intravital microscopy. *Microcirculation* 4:233–252.
23. Hudetz AG. (2003). The cerebral microcirculation in ischemia and hypoxemia: the Arisztid G. B. Kovach Memorial Lecture. *Adv Exp Med Biol* 530:347–357.
24. Hyde JS, Biswal BB, Jesmanowicz A. (2001). High-resolution fMRI using multislice partial k-space GR-EPI with cubic voxels. *Magn Reson Med* 46:114–125.
25. Ivanov KP, Kalinina MK, Levkovich Yu I. (1981). Blood flow velocity in capillaries of brain and muscles and its physiological significance. *Microvasc Res* 22:143–155.
26. Karau KL, Molthen RC, Dhyani A, Haworth ST, Hanger CC, Roerig DL, Johnson RH, Dawson CA. (2001). Pulmonary arterial morphometry from microfocal X-ray computed tomography. *Am J Physiol Heart Circ Physiol* 281:H2747–H2756.
27. Kassab GS, Rider CA, Tang NJ, Fung YC. (1993). Morphometry of pig coronary arterial trees. *Am J Physiol* 265:H350–H365.
28. Kassab GS, Lin DH, Fung YC. (1994). Morphometry of pig coronary venous system. *Am J Physiol* 267:H2100–H2113.
29. Kassab GS. (2000). The coronary vasculature and its reconstruction. *Ann Biomed Eng* 28:903–915.
30. Kayar SR, Archer PG, Lechner AJ, Banchero N. (1982). The closest-individual method in the analysis of the distribution of capillaries. *Microvasc Res* 24:326–341.
31. Kirchner LM, Schmidt SP, Gruber BS. (1996). Quantitation of angiogenesis in the chick chorioallantoic membrane model using fractal analysis. *Microvasc Res* 51:2–14.
32. Lauwers F, Cassot F, Marc-Vergnes JP, Moscovici J, Guitard J. (2000) Approche morphometrique de la microcirculation du cortex cerebral humain. *Morphologie* 267:31–32 (Abstr).
33. Lazorthes G, Espagno J, Lazorthes Y, Zadeh JO. (1968). The vascular architecture of the cortex and the cortical blood flow. *Prog Brain Res* 30:27–32.
34. Lazorthes G, Gouaze A. (1976). *Vascularisation et Circulation de l'Encephale*, Tome 1. Paris: Masson.
35. le Noble F, Fleury V, Pries A, Corvol P, Eichmann A, Reneman RS. (2005). Control of arterial branching morphogenesis in embryogenesis: go with the flow. *Cardiovasc Res* 65:619–628.
36. Levy BI, Ambrosio G, Pries AR, Struijker-Boudier HA. (2001). Microcirculation in hypertension: a new target for treatment? *Circulation* 104:735–740.
37. Logothetis NK, Pauls J, Augath M, Trinath T, Oeltermann A. (2001). Neurophysiological investigation of the basis of the fMRI signal. *Nature* 412:150–157.
38. Masters BR. (2004). Fractal analysis of the vascular tree in the human retina. *Annu Rev Biomed Eng* 6:427–452.
39. McKeefry DJ, Zeki S. (1997). The position and topography of the human colour center as revealed by functional magnetic resonance imaging. *Brain* 120 (Pt 12):2229–2242.
40. Minnich B, Leeb H, Bernroider EW, Lametschwandtner A. (1999). Three-dimensional morphometry in scanning electron microscopy: a technique for accurate dimensional and angular measurements of microstructures using stereopaired digitized images and digital image analysis. *J Microsc* 195 (Pt 1):23–33.
41. Minnich B, Bartel H, Lametschwandtner A. (2001). Quantitative microvascular corrosion casting by 2D- and 3D-morphometry. *Ital J Anat Embryol* 106:213–220.
42. Mironov V, Hritz MA, LaManna JC, Hudetz AG, Harik SI. (1994). Architectural alterations in rat cerebral microvessels after hypobaric hypoxia. *Brain Res* 660:73–80.
43. Motti ED, Imhof HG, Yasargil MG. (1986). The terminal vascular bed in the superficial cortex of the rat: an SEM study of corrosion casts. *J Neurosurg* 65:834–846.
44. Pawlik G, Rackl A, Bing RJ. (1981). Quantitative capillary topography and blood flow in the cerebral cortex of cats: an in vivo microscopic study. *Brain Res* 208:35–58.
45. Pittman R. (1995). Influence of microvascular architecture on oxygen exchange in skeletal muscle. *Microcirculation* 2:1–18.
46. Pittman R. (2005). Oxygen transport and exchange in the microcirculation. *Microcirculation* 12:59–70.
47. Plouraboue F, Cloetens P, Fonta C, Steyer A, Lauwers F, Marc-Vergnes JP. (2004). X-ray high-resolution vascular network imaging. *J Microsc* 215:139–148.
48. Popel AS, Pries AR, Slaaf DW. (1999). Microcirculation Physiome Project. *J Vasc Res* 36:253–255.
49. Pries AR, Neuhaus D, Gaehtgens P. (1992). Blood viscosity in tube flow: dependence on diameter and hematocrit. *Am J Physiol* 263:H1770–H1778.
50. Pries AR, Reglin B, Secomb TW. (2001). Structural adaptation of microvascular networks: functional

roles of adaptive responses. *Am J Physiol Heart Circ Physiol* 281:H1015–H1025.
51. Pries AR, Reglin B, Secomb TW. (2003). Structural response of microcirculatory networks to changes in demand: information transfer by shear stress. *Am J Physiol Heart Circ Physiol* 284:H2204–H2212.
52. Pries AR, Secomb TW. (2005). Control of blood vessel structure: insights from theoretical models. *Am J Physiol Heart Circ Physiol* 288:H1010–H1015.
53. Pudney C. (1998). Distance-ordered homotopic thinning: a skeletonization algorithm for 3D digital images. *Computer Vision and Image Understanding* 72:404–413.
54. Reina-De La Torre F, Rodriguez-Baeza A, Sahuquillo-Barris J. (1998). Morphological characteristics and distribution pattern of the arterial vessels in human cerebral cortex: a scanning electron microscope study. *Anat Rec* 251:87–96.
55. Rodriguez-Baeza A, Reina-De La Torre F, Ortega-Sanchez M, Sahuquillo-Barris J. (1998). Perivascular structures in corrosion casts of the human central nervous system: a confocal laser and scanning electron microscope study. *Anat Rec* 252:176–184.
56. Sabo E, Boltenko A, Sova Y, Stein A, Kleinhaus S, Resnick MB. (2001). Microscopic analysis and significance of vascular architectural complexity in renal cell carcinoma. *Clin Cancer Res* 7:533–537.
57. Secomb TW, Hsu R, Pries AR. (2002). Blood flow and red blood cell deformation in nonuniform capillaries: effects of the endothelial surface layer. *Microcirculation* 9:189–196.
58. Secomb TW, Hsu R, Park EY, Dewhirst MW. (2004). Green's function methods for analysis of oxygen delivery to tissue by microvascular networks. *Ann Biomed Eng* 32:1519–1529.
59. Sobin SS, Fung YC, Lindal RG, Tremer HM, Clark L. (1980). Topology of pulmonary arterioles, capillaries, and venules in the cat. *Microvasc Res* 19:217–233.
60. Stalling D, Westerhoff M, Hege H.C. (2005) Amira: a highly interactive system for visual data analysis. In: *The Visualization Handbook* (CD Hansen, CR. Johnson, Eds.) Elsevier. Toulouse. 749–767.
61. Tata DA, Anderson BJ. (2002). A new method for the investigation of capillary structure. *J Neurosci Methods* 113:199–206.
62. Turcotte DL, Pelletier JD, Newman WI. (1998). Networks with side branching in biology. *J Theor Biol* 193:577–592.
63. Turner R. (2002). How much cortex can a vein drain? Downstream dilution of activation-related cerebral blood oxygenation changes. *Neuroimage* 16:1062–1067.
64. Vico PG, Kyriacos S, Heymans O, Louryan S, Cartilier L. (1998). Dynamic study of the extraembryonic vascular network of the chick embryo by fractal analysis. *J Theor Biol* 195:525–532.
65. Yen RT, Zhuang FY, Fung YC, Ho HH, Tremer H, Sobin SS. (1983). Morphometry of cat pulmonary venous tree. *J Appl Physiol* 55:236–242.
66. Zakrzewicz A, Secomb TW, Pries AR. (2002). Angioadaptation: keeping the vascular system in shape. *News Physiol Sci* 17:197–201.

APPENDIX A: CENTERLINES EXTRACTION METHODS

Overall Method

Extracting vessel center lines consists in the following steps: a threshold that separates vessels (in white) from the background (in black); distance map computation that computes for each vessel's point its shortest distance to the background; thinning to determine points belonging to center lines; joining center line points into lines; adding to each center line point the vessel radius at this point (which corresponds to its shortest distance to the background). The threshold is chosen manually by experts on the whole mosaic (the lost of luminosity has been compensated on lowest slides).

Distance Map Computation

Numerous ways have been investigated to compute distance maps. Chamfer transforms, popularized by Borgefors (9), achieve a good trade-off between precision and computational cost. They propagate local integer distances using chamfer masks. Roughly speaking, a chamfer mask is a set of legal displacements weighted by local distances. A distance between two points is generally defined as the length of the shortest path between these points. In the case of chamfer distance, we reduce the path choice to linear combinations of the legal displacements allowed by the mask. To obtain a chamfer distance as close as possible to the Euclidean one, we can, on one side, allow more paths, which means increasing mask size, and on the other side, carefully choose the mask coefficients leading to the smallest error with respect to the Euclidean distance. The first way is the easiest, but increases the chamfer map computational cost. The second way is the most challenging. This computation is generally done on isotropic grids. In our case, however, slice thickness is larger than pixel size. We thus take into account the anisotropy of the lattice and consider the use of adapted coefficients computation methods (14).

Thinning Method

To determine vessel center lines, we can consider either medial axis or skeleton. A medial axis can be

defined as a set that is thin and centered within the object. The skeleton of an object is thin and topologically equivalent to this object. In our case, the topology is the most significant property we want to preserve to characterize and model the microvascular network. We thus consider homotopic skeletons. Moreover, as we also aim at computing vessels diameters, we want the skeleton to be centered within vessels. More precisely, we want the skeleton to be homotopic (i.e., topologically equivalent to the original object), thin (i.e., one voxel wide), and centered with respect to the original object.

A skeleton can be built in the continuous space through Voronoi diagrams or partial derivative equations. However, continuous methods have huge computational costs and often raise difficulties when applied to discrete images. This leads us to considering discrete methods, which can be based on the following:

- *Thinning*: The skeleton is computed by iteratively peeling off the boundary of the object, layer by layer. It consists of the iterative deletion of simple points (a point is said to be simple if and only if its deletion does not alter the object topology). A point can be characterized as simple by examining its neighborhood. This method ensures that we obtain a homotopic skeleton.
- *Distance maps*: The skeleton is defined as the locus of the local maxima of the distance map. The resulting skeleton is thin and centered, but not necessarily homotopic with respect to the original object.

Hybrid methods have been recently introduced to take advantage of both approaches (53). These methods are called distance ordered homotopic thinning (DOHT). They use a distance map to guide the process of iteratively removing simple points (homotopic thinning) toward the center of the object. They thus lead to a skeleton that is homotopic, thin, and centered with respect to the original object.

However, the DOHT algorithm supposes that the image can be loaded and processed at once in the memory of a standard computer. If we process independently on image blocks, center line disconnections appear on block borders. We propose to adapt DOHT to a blockwise process. This adaptation is driven by the skeleton properties we want to preserve:

- *Homotopy* can be guaranteed by deleting only simple points of the object. A point can be guaranteed to be simple by investigating its neighborhood. Problems of homotopy appear on block borders because neighborhoods of points located on block borders are partially unknown. To solve this problem, we freeze points located on block borders; i.e., we delete a point only if its whole neighbourhood is included within the block. This condition guarantees a homotopic skeleton.
- *Medialness* is a regional property that is no more verified if we only freeze points on the one-voxel border as proposed above. Indeed, in the case of a vessel crossing 2 blocks, the obtained skeleton is *stuck* to the border of the first thinned block and no more located at the object center. To overcome this problem, we delete a simple point only if its distance to the block border is larger than its distance to the object border. This means that a point can be deleted only if its associated maximal ball is entirely included within the block. This ensures that points of the expected skeleton, which are supposed to be on maxima balls centers, are kept.
- *Thinness*: The two previous conditions lead to a homotopic and potentially medial skeleton. But it may remain thick. Indeed, object areas located on block borders have not entirely been thinned. To obtain a thin skeleton, we reapply the skeletonization algorithm with the same conditions, but on the area that remained thick, that is to say the block borders.

We thus obtain a skeleton, which is *homotopic*, *centered*, and *thin* with respect to the vessels network.

Vessels Representation

We then reconstruct lines by considering the connectivity of the obtained skeleton points, and affect to each line point its corresponding value in the distance map. This value represents the shortest distance from the vessel center to the background, that is to say, its radius at this point.

Vessels are stored as a set of lines made of sets of points added with corresponding radii. They can be represented as cylinder sets centered on center line points with diameters corresponding to the vessels diameter at this point.

These algorithms have been included in the "MicroVisu3D" extension of the 3D visualization package Amira (Mercury TGS, Merignac-France, San Diego, CA, USA, Zuse Institute, Berlin, Germany).